Aalto University

Blinov, D.; Pavlidou, V.; Papadakis, I. E.; Hovatta, T.; Pearson, T. J.; Liodakis, I.; Panopoulou, G. V.; Angelakis, E.; Baloković, M.; Das, H.; Khodade, P.; Kiehlmann, S.; King, O. G.; Kus, A.; Kylafis, N.; Mahabal, A.; Marecki, A.; Modi, D.; Myserlis, I.; Paleologou, E.; Papamastorakis, I.; Pazderska, B.; Pazderski, E.; Rajarshi, C.; Ramaprakash, A.; Readhead, A. C S; Reig, P.; Tassis, K.; Zensus, J. A.

RoboPol

Please cite the original version:
Blinov, D., Pavlidou, V., Papadakis, I. E., Hovatta, T., Pearson, T. J., Liodakis, I., Panopoulou, G. V., Angelakis, E., Balokovi, M., Das, H., Khodade, P., Kiehlmann, S., King, O. G., Kus, A., Kylafis, N., Mahabal, A., Marecki, A., Modi, D., Myserlis, I., ... Zensus, J. A. (2016). RoboPol: Optical polarization-plane rotations and flaring activity in blazars. *Monthly Notices of the Royal Astronomical Society*, *457*(2), 2252-2262. https://doi.org/10.1093/mnras/stw158

RoboPol: optical polarization-plane rotations and flaring activity in blazars

D. Blinov,[1,2,3]★ V. Pavlidou,[1,2] I. E. Papadakis,[1,2] T. Hovatta,[4] T. J. Pearson,[5]
I. Liodakis,[1,2] G. V. Panopoulou,[1] E. Angelakis,[6] M. Baloković,[5] H. Das,[7] P. Khodade,[7]
S. Kiehlmann,[4] O. G. King,[5] A. Kus,[8] N. Kylafis,[2,1] A. Mahabal,[5] A. Marecki,[8]
D. Modi,[7] I. Myserlis,[6] E. Paleologou,[1] I. Papamastorakis,[1,2] B. Pazderska,[8]
E. Pazderski,[8] C. Rajarshi,[7] A. Ramaprakash,[7] A. C. S. Readhead,[5] P. Reig,[1,2]
K. Tassis[1,2] and J. A. Zensus[6]

[1]*Department of Physics, Institute for Plasma Physics, University of Crete, GR-71003, Heraklion, Greece*
[2]*Foundation for Research and Technology – Hellas, IESL, Voutes, GR-71110 Heraklion, Greece*
[3]*Astronomical Institute, St. Petersburg State University, Universitetsky pr. 28, Petrodvoretz, 198504 St. Petersburg, Russia*
[4]*Aalto University Metsähovi Radio Observatory, Metsähovintie 114, FI-02540 Kylmälä, Finland*
[5]*Cahill Center for Astronomy and Astrophysics, California Institute of Technology, 1200 E California Blvd, MC 249-17, Pasadena CA, 91125, USA*
[6]*Max-Planck-Institut für Radioastronomie, Auf dem Hügel 69, D-53121 Bonn, Germany*
[7]*Inter-University Centre for Astronomy and Astrophysics, Post Bag 4, Ganeshkhind, Pune-411 007, India*
[8]*Toruń Centre for Astronomy, Nicolaus Copernicus University, Faculty of Physics, Astronomy and Informatics, Grudziadzka 5, PL-87-100 Toruń, Poland*

ABSTRACT

We present measurements of rotations of the optical polarization of blazars during the second year of operation of RoboPol, a monitoring programme of an unbiased sample of gamma-ray bright blazars specially designed for effective detection of such events, and we analyse the large set of rotation events discovered in two years of observation. We investigate patterns of variability in the polarization parameters and total flux density during the rotation events and compare them to the behaviour in a non-rotating state. We have searched for possible correlations between average parameters of the polarization-plane rotations and average parameters of polarization, with the following results: (1) there is no statistical association of the rotations with contemporaneous optical flares; (2) the average fractional polarization during the rotations tends to be lower than that in a non-rotating state; (3) the average fractional polarization during rotations is correlated with the rotation rate of the polarization plane in the jet rest frame; (4) it is likely that distributions of amplitudes and durations of the rotations have physical upper bounds, so arbitrarily long rotations are not realized in nature.

Key words: polarization – galaxies: active – galaxies: jets – galaxies: nuclei.

1 INTRODUCTION

Blazars are extreme active galactic nuclei with relativistic jets oriented towards the Earth. The close alignment of the jet to the line of sight leads to relativistic boosting of the jet emission, which dominates the overall emission. The broad-band spectral energy distribution (SED) of a blazar typically exhibits two broad humps. The low-energy part of SED, which peaks in the sub-millimetre to UV/X-ray range, is produced by synchrotron emission from relativistic electrons in the jet. Owing to its synchrotron nature, the optical emission of blazars is often significantly polarized (Angel & Stockman 1980).

Typically, a blazar's electric vector position angle (EVPA) shows erratic variations in the optical band (Moore et al. 1982; Uemura et al. 2010). However, the EVPA occasionally undergoes continuous and smooth rotations that sometimes occur simultaneously with flares in the broad-band emission (Marscher et al. 2008).

The RoboPol programme[1] has been designed for an efficient detection of the EVPA rotations in a sample of blazars that allows statistically rigorous studies of this phenomenon. For this purpose, we

---

★ E-mail: blinov@physics.uoc.gr

[1] http://robopol.org

have selected the monitoring sample on the basis of bias-free, strict and objective criteria (Pavlidou et al. 2014). We have secured a considerable amount of evenly allocated telescope time over a period of many months for three years, we have constructed a specifically designed polarimeter, and we have developed an automated system for the telescope operation and data reduction (King et al. 2014).

RoboPol started observations at Skinakas observatory in 2013 May. The EVPA rotations detected during its first season of operation were presented in Blinov et al. (2015, hereafter Paper I). In that paper, we examined the connection between the EVPA rotation events and gamma-ray flaring activity in blazars. We found it to be highly likely that at least some EVPA rotations are physically connected to the gamma-ray flaring activity. We also found that the most prominent gamma-ray flares occur simultaneously with the EVPA rotations, while relatively faint flares may have a negative or positive time lag. This was interpreted as possible evidence for the existence of two separate mechanisms responsible for the EVPA rotations.

In this paper, we present the new set of EVPA rotations that we detected during the second RoboPol observing season in 2014. We focus on the optical observational data, and we study the statistical properties of the detected EVPA rotations in both observing seasons. We aim to determine the average parameters of the rotations, and test possible correlations between these parameters as well as the average total flux density and fractional polarization. The investigation of statistical regularities and correlations may provide important clues to the physical processes that produce EVPA rotations in the emission of blazars.

After a brief description of the monitoring programme, observing and reduction techniques in Section 2, we present the EVPA rotations detected by RoboPol during the second season. In Sections 3 and 4, characteristics of the entire set of rotations are analysed and a number of possible correlations between parameters of EVPA rotations and polarization properties are studied. Our findings are summarized in Section 5.

2 OBSERVATIONS, DATA REDUCTION AND DETECTED EVPA ROTATIONS

The second RoboPol observing run started in 2014 April and lasted until the end of 2014 November. During the seven-month period, we obtained 1177 measurements of objects from our monitoring sample. The observations of each object were almost uniformly spread out over the period during which the object was observable.

2.1 Data analysis

All the polarimetric and photometric data analysed in this paper were obtained at the 1.3 m telescope of Skinakas observatory[2] using the RoboPol polarimeter. The polarimeter was specifically designed for this monitoring programme, and it has no moving parts besides the filter wheel. As a result, we avoid unmeasurable errors caused by sky changes between measurements and the non-uniform transmission of a rotating optical element. The features of the instrument as well as the specialized pipeline with which the data were processed are described in King et al. (2014).

The data presented in this paper were taken with the *R*-band filter. Magnitudes were calculated using calibrated field stars either found in the literature or presented in the Palomar Transient Factory

catalogue (Ofek et al. 2012) or the USNO-B1.0 catalogue (Monet et al. 2003), depending on availability. Photometry of blazars with bright host galaxies was performed with a constant 6 arcsec aperture. All other sources were measured with an aperture defined as 2.5 × FWHM, where FWHM is an average full width at half-maximum of stellar images, which has a median value of 2.1 arcsec.

The exposure time was adjusted according to the brightness of each target, which was estimated during a short pointing exposure. Typical exposures for targets in our sample were in the range 2–30 min. The average relative photometric error was ∼0.04 mag. Objects in our sample have Galactic latitude $|b| > 10°$ (see Pavlidou et al. 2014), so the average colour excess in the directions of our targets is relatively low, $\langle E(B - V)\rangle = 0.11$ mag (Schlafly & Finkbeiner 2011). Consequently, the interstellar polarization is expected to be less than 1.0 per cent, on average, according to Serkowski, Mathewson & Ford (1975). The statistical uncertainty in the measured degree of polarization is less than 1 per cent in most cases, while the EVPA is typically determined with a precision of $1°–10°$ depending on the source brightness and fractional polarization.

2.2 Definition of an EVPA rotation

We accept a swing between two consecutive EVPA measurements $\Delta\theta = |\theta_{n+1} - \theta_n|$ as significant, if $\Delta\theta > \sqrt{\sigma(\theta_{n+1})^2 + \sigma(\theta_n)^2}$. In order to resolve the 180° ambiguity of the EVPA, we followed a standard procedure (see e.g. Kiehlmann et al. 2013), which is based on the assumption that temporal variations of the EVPA are smooth and gradual, hence adopting minimal changes of the EVPA between consecutive measurements. We define the EVPA variation as $\Delta\theta_n = |\theta_{n+1} - \theta_n| - \sqrt{\sigma(\theta_{n+1})^2 + \sigma(\theta_n)^2}$, where θ_{n+1} and θ_n are the $n+1$ and nth points of the EVPA curve and $\sigma(\theta_{n+1})$ and $\sigma(\theta_n)$ are the corresponding uncertainties of the position angles. If $\Delta\theta_n > 90°$, we shift the angle θ_{n+1} by $\pm k \times 180°$, where the integer $\pm k$ is chosen in such a way that it minimizes $\Delta\theta_n$. If $\Delta\theta_n \leq 90°$, we leave θ_{n+1} unchanged.

There is no objective physical definition of an EVPA rotation. Strictly speaking, any significant change of the EVPA between two measurements constitutes a rotation. However, typically only high-amplitude ($>90°$), smooth and well-sampled variations of the EVPA are considered as rotations in the literature. As in Paper I, we define as an EVPA rotation any continuous change of the EVPA curve with a total amplitude of $\Delta\theta_{max} \geq 90°$, which is comprised of at least four measurements with at least three significant swings between them. The start and end points of a rotation event are defined by a change of the EVPA curve slope $\Delta\theta_n/\Delta t_n$ by a factor of 5 or a significant change of its sign. This definition is rather conservative, and is in general consistent with rotations reported in the literature.

2.3 Detected EVPA rotations

In the data set obtained during the second observing season, we identified 11 events in 10 blazars of the main sample that follow our adopted definition of an EVPA rotation. The observational characteristics of rotations are their duration, T_{rot}, amplitude, $\Delta\theta_{max}$, and average rate of the EVPA variability, $\langle\Delta\theta/\Delta T\rangle = \Delta\theta_{max}/T_{rot}$. These parameters for the rotations detected during the second season are listed in Table 1, together with the observing season length, T_{obs}, the median cadence of observations, $\langle\Delta t\rangle$, the redshift, z, and the Doppler factor, δ, for the corresponding blazar. The last two parameters are necessary in order to translate an observed time interval, Δt_{obs}, to the jet's reference frame, Δt_{jet}, according to the

Table 1. Observational data for EVPA rotations detected by RoboPol in 2014. Columns (1), (2): blazar identifiers; (3): redshift; (4): 2014 observing season length/median time difference between consecutive observations; (5): total amplitude of EVPA change; (6): duration of the rotation/number of observations during rotation; (7): average rotation rate; (8): Doppler factor; (9): blazar subclass (LBL, IBL, HBL denote low, intermediate and high synchrotron peaked BL Lacertae objects, LPQ – low-peaked flat-spectrum radio quasar).

Blazar ID	Survey name	z	$T_{obs}/\langle \Delta t \rangle$ (d)/(d)	$\Delta\theta_{max}$ (deg)	T_{rot}/N_{rot} (d)	$\langle \Delta\theta/\Delta T \rangle$ (deg d^{-1})	δ	Class
RBPL J0136+4751	OC 457	0.859[1]	135.7/6.5	−91.8	41.8/5	−2.2	20.7[2]	LPQ[1]
RBPL J1037+5711	GB6 J1037+5711	–	53.9/3.0	−165.3	31.0/6	−5.3	–	IBL[1]
RBPL J1512−0905	PKS 1510−089	0.360[1]	137.8/3.0	242.6	14.1/7	17.3	16.7[2]	LPQ[1]
RBPL J1512−0905	−″−	−″−	−″−	−199.2	11.0/6	−18.2	−″−	−″−
RBPL J1555+1111	PG 1553+113	–	154.7/4.0	144.7	19.0/5	7.6	–	HBL[1]
RBPL J1748+7005	S4 1749+70	0.770[1]	188.7/4.0	−126.4	39.0/14	−3.2	–	IBL[1]
RBPL J1751+0939	OT 081	0.322[1]	176.6/6.0	−335.1	32.0/10	−10.5	12.0[2]	LBL[1]
RBPL J1800+7828	S5 1803+784	0.680[1]	144.7/4.5	−191.7	32.0/7	−6.0	12.2[2]	LBL[1]
RBPL J1806+6949	3C 371	0.051[1]	185.7/8.0	−186.5	63.0/6	−3.0	1.1[2]	LBL[3], IBL[1]
RBPL J2022+7611	S5 2023+760	0.594[4]	101.7/8.5	107.3	23.0/4	−4.7	–	IBL[1]
RBPL J2253+1608	3C 454.3	0.859[1]	157.7/10.0	144.7	8.9/5	16.3	33.2[2]	LPQ[1]

Notes. [1]Richards et al. (2014); [2]Hovatta et al. (2009); [3]Ghisellini et al. (2011); [4]Shaw et al. (2013).
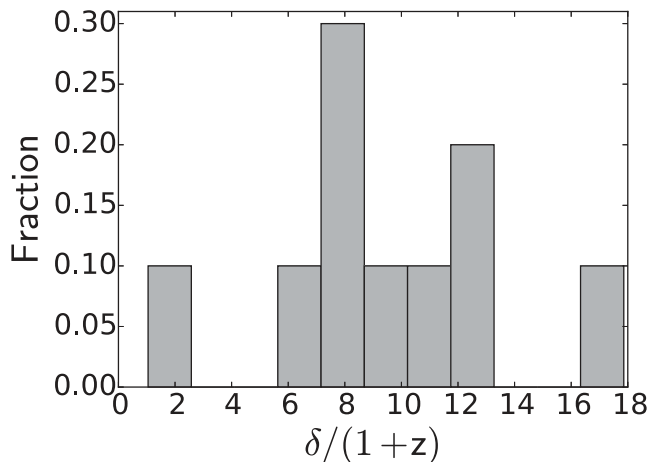
Figure 1. Distribution of $\delta/(1 + z)$ for blazars with detected rotations.

Figure 2. Season length, T_{obs}, and median cadence, $\langle \Delta t \rangle$, for blazars with detected rotations for both observing seasons. The lines border areas inside which rotations slower than 9 and 20 deg d^{-1} can be detected (see the text for details).

relation $\Delta t_{jet} = \Delta t_{obs}\delta/(1 + z)$. The distribution of $\delta/(1 + z)$ factors for the blazars with detected rotations is shown in Fig. 1. It ranges between 1.05 and 17.86, and cannot be distinguished from a uniform distribution with this range by a Kolmogorov–Smirnov (K–S) test (*p*-value = 0.34). Hereafter in this paper, for uniformity (normality) tests, we compare the observed distribution with the uniform (normal) distribution which has the same range (mean and standard deviation) as the observed one. Throughout this paper, we use the Doppler factors estimated by Hovatta et al. (2009) from the variability of the total flux density at 37 GHz, which are the most reliable and consistent Doppler factor estimates available. However, it is possible that the actual Doppler factors for the optical emission region may be significantly different, for the following reasons: (1) it has not been firmly established that the optical emission is co-spatial with the centimetre-wavelength radio core, although there are some suggestions that it is (e.g. Gabuzda et al. 2006); (2) they were obtained for a different observing period; (3) they were calculated assuming energy equipartition between the magnetic field and the radiating particles (Readhead 1994; Lähteenmäki & Valtaoja 1999), which may be incorrect (e.g. Gómez et al. 2016).

In Fig. 2, we show $\langle \Delta t \rangle$ versus T_{obs} for the blazars with detected rotations in the 2013 and 2014 seasons. In total, we have detected 27 EVPA rotations in 20 blazars, all of which are gamma-ray-loud objects. This is 20 per cent of the sample we monitor. Three blazars
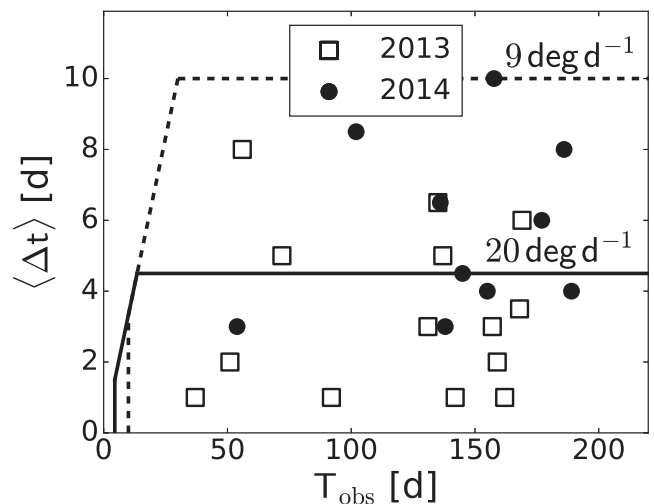
have shown two rotations and one has shown three rotations during the monitoring period. The lines in Fig. 2 bound regions ('detection boxes') in the $\langle \Delta t \rangle$–T_{obs} plane, where a rotation slower than a given rate could have been detected (see discussion in Section 3.3 of Paper I). For example, the solid line in Fig. 2 indicates the maximum $\langle \Delta t \rangle$ value, for any given duration of observations, T_{obs}, that is necessary in order to detect rotations with a rate of $\langle \Delta\theta/\Delta T \rangle$ smaller than 20 deg d^{-1}, on average. We are confident that we could detect rotations with $\langle \Delta\theta/\Delta T \rangle < 20$ deg d^{-1} for all the blazars within the 20 deg d^{-1} detection box.

The full season EVPA curves along with the evolution of the polarization degree and the *R*-band flux density, for the 10 blazars with rotations detected in 2014, are shown in Fig. 3. The EVPA rotation intervals are marked by filled black points. Clearly, the events we have considered as rotations based on our criteria are the largest $\Delta\theta_{max}$ rotation events that appear in these data sets. They are all characterized by smooth variations with a well-defined trend.
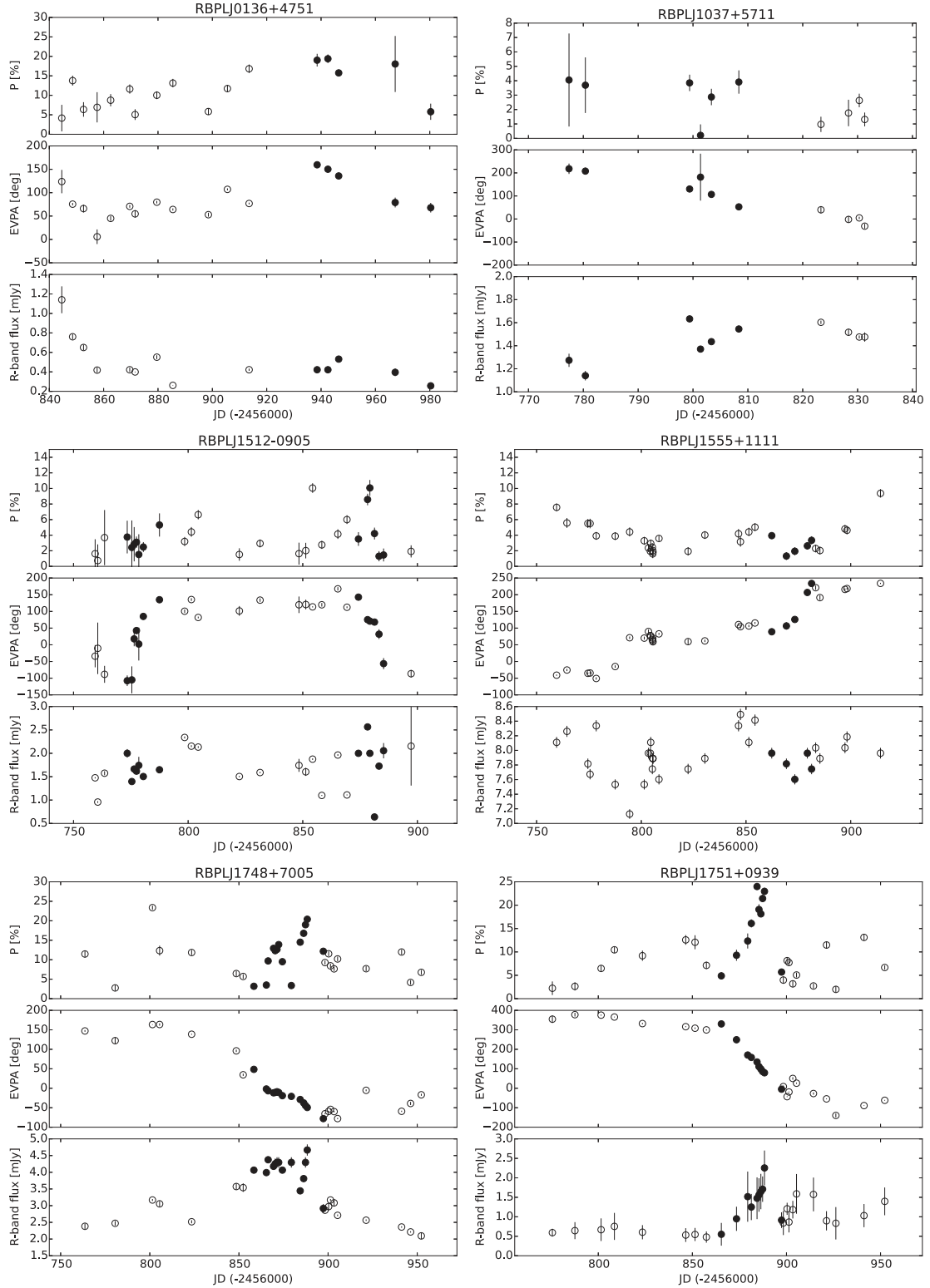
Figure 3. Evolution of polarization degree, polarization position angle and *R*-band flux density for blazars with a detected rotation in the second RoboPol season. Periods of rotations are marked by filled black points.

3 PROPERTIES OF THE EVPA ROTATIONS

Here we present the distributions of the observational parameters of the rotations, namely $\Delta\theta_{max}$, T_{rot}, and $\langle\Delta\theta/\Delta T\rangle$, and study their properties.

Fig. 2 shows that the median cadence, $\langle\Delta t\rangle$, spans a range between $\sim$1 and 10 d, and the duration of observations, T_{obs} spans $\sim$ 40–200 d. Since our ability to detect an EVPA rotation with a specific rate depends on $\langle\Delta t\rangle$ and T_{obs}, the observed rotations may not
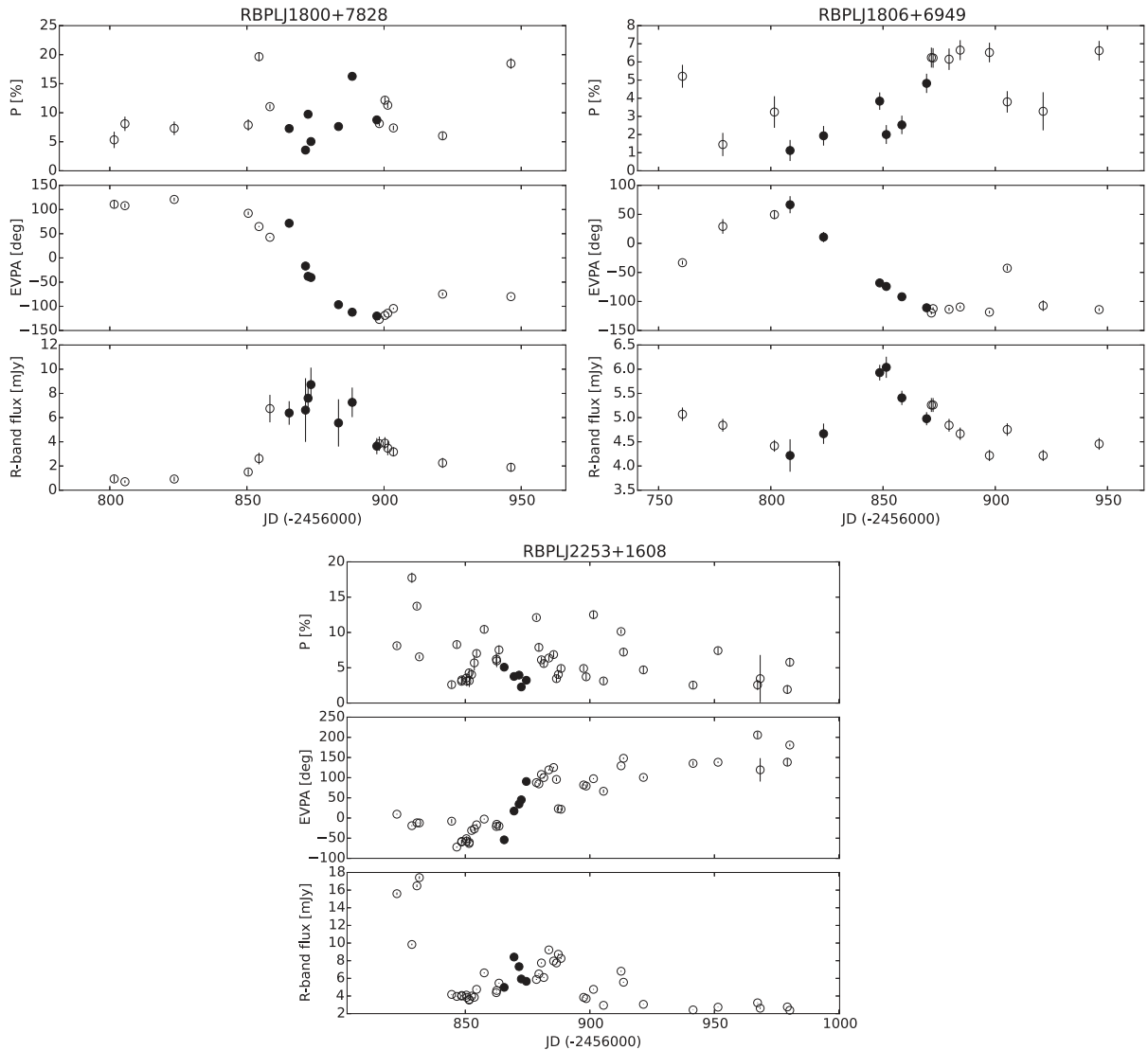
Figure 3 – *continued.*

constitute an unbiased sample of the intrinsic population of EVPA rotations. For this reason, in addition to the sample of all the rotations detected so far ('full sample' hereafter), we also considered a 'complete' sample of rotations, which consists of all the detected rotations with $\langle \Delta\theta/\Delta T \rangle < 20$ deg d^{-1}, but only for those objects that are located within the 20 deg d^{-1} detection box in Fig. 2. In other words, our 'complete' sample consists of all the rotations with $\langle \Delta\theta/\Delta T \rangle < 20$ deg d^{-1} detected in these objects, where we could not have missed them.

A choice of a limit lower than 20 deg d^{-1} would result in an increase of the number of blazars (see Fig. 2), but a decrease in the number of rotations in the sample (as we would have missed the 'faster' ones – see Table 1). The limit of 20 deg d^{-1} maximizes the number of rotations in the 'complete' sample, detected in blazars with known redshift and Doppler factor. In any case, our results are not sensitive to the rotation rate limit. There are 16 rotations in the 'complete' sample, compared to 27 in the full sample.

3.1 Distribution of $\Delta\theta_{max}$

Fig. 4 shows the $\Delta\theta_{max}$ distribution for the full and complete samples (left-hand and right-hand panels, respectively). The longest EVPA rotation observed by RoboPol so far has $\Delta\theta_{max} = 347°$. The longest rotation reported in the literature has $\Delta\theta_{max} = 720°$ (Marscher et al. 2010), although Sasada et al. (2011) considered it to be two rotations, with the longer one having $\Delta\theta_{max} \sim 500°$. The break at the lower end of the distributions in Fig. 4 is due to our definition of an EVPA rotation, which requires $\Delta\theta_{max} \geq 90°$.

The parameters of the full and complete $\Delta\theta_{max}$ distributions are almost identical: mean = 186°, $\sigma = 69°$ (full), and 187°, 69° (complete). According to the K–S test, the $\Delta\theta_{max}$ distributions could be drawn from a normal or from a uniform distribution. The corresponding p-values are p-norm = 0.96, p-unif = 0.087 for the full sample and p-norm = 0.95, p-unif = 0.28 for the complete sample.
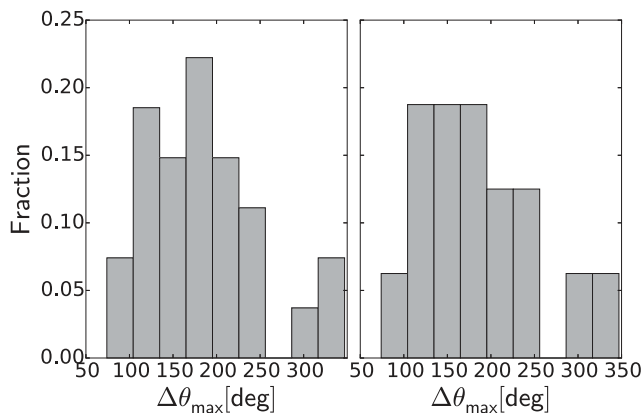
Figure 4. Distributions of $\Delta\theta_{\mathrm{max}}$ for the full sample (left) and the complete sample (right).
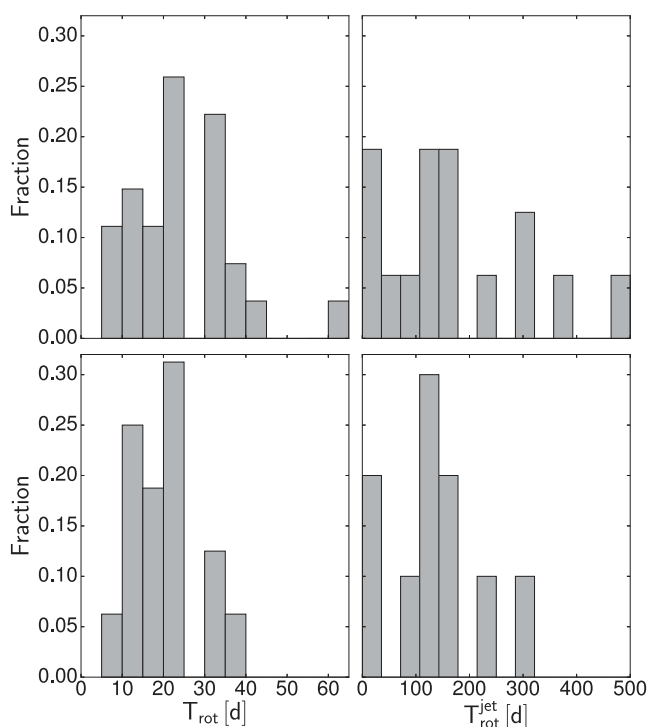

Figure 5. Distributions of T_{rot} for the full sample (top) and the complete sample (bottom) plotted in the observer frame (left-hand column) and the jet reference frame (right-hand column).

3.2 Distribution of T_{rot}

Fig. 5 shows the distribution of rotation duration, T_{rot}, for the full and complete samples (top and bottom panels, respectively), in both the observer and jet reference frames (left-hand and right-hand panels, T_{rot} and $T_{\mathrm{rot}}^{\mathrm{jet}}$, respectively). The lower bound of $T_{\mathrm{rot}} = 5$ d in both samples is presumably caused by selection effects. There are signs of very fast rotations in our data, but they require a cadence of observations much shorter than the typical $\langle \Delta t \rangle$ in our sample to be confidently detected. The distributions of $T_{\mathrm{rot}}^{\mathrm{obs}}$ in the observer frame are consistent with the normal distribution, for both the full and the complete samples. The corresponding K–S test p-values are p-norm = 0.59, p-unif = 0.002 and p-norm = 0.56, p-unif = 0.07. The parameters of the $T_{\mathrm{rot}}^{\mathrm{obs}}$ distribution for the full sample (mean = 24.4 d, σ = 12.3 d) are close to those for the complete sample
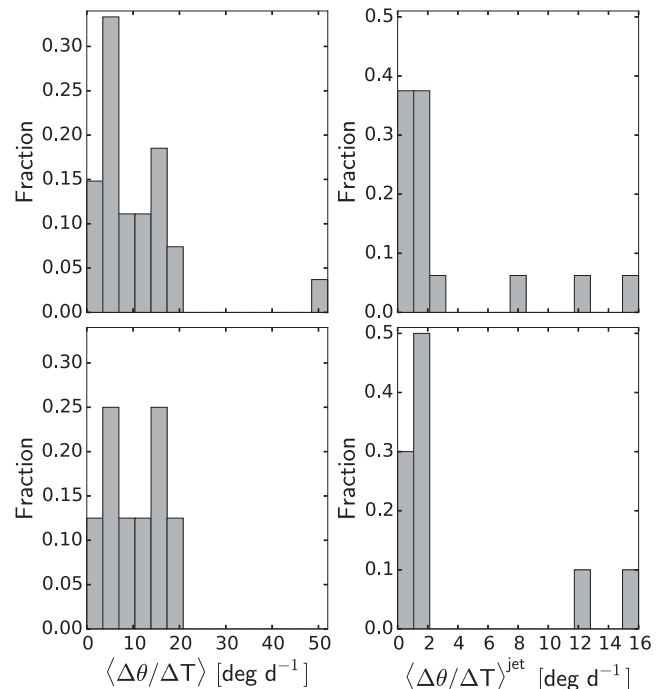

Figure 6. Distributions of $\langle \Delta\theta/\Delta T \rangle$ for the full sample (top) and the complete sample (bottom). The observer reference frame is shown in the left-hand column and the jet frame in the right-hand column.

(mean = 20.5 d, σ = 8.1 d). The distributions of $T_{\mathrm{rot}}^{\mathrm{jet}}$ in the full and complete samples appear to be more uniform than the observed ones. However, they cannot be confidently distinguished from either the normal or the uniform distributions. The corresponding p-values are p-norm = 0.59, p-unif = 0.04 and p-norm = 0.996, p-unif = 0.49. The minimum and maximum $T_{\mathrm{rot}}^{\mathrm{jet}}$ are 19 and 465 d for the full, and 19 and 299 d for the complete sample.

3.3 Distribution of $\langle \Delta\theta/\Delta T \rangle$

Fig. 6 shows $\langle \Delta\theta/\Delta T \rangle$ for the full (top panels) and complete samples (bottom panels), in both the observer (left-hand column) and jet reference frames (right-hand column). The limited cadence of observations biases the $\langle \Delta\theta/\Delta T \rangle$ distribution for the full sample. Presumably for this reason, the observed $\langle \Delta\theta/\Delta T \rangle$ distribution for the full sample is strongly non-uniform, but it cannot be distinguished from a normal distribution (p-norm = 0.28, p-unif = 4 $\times$ 10^{-11}). However, in the complete sample, $\langle \Delta\theta/\Delta T \rangle$ is likely to be distributed uniformly (p-norm = 0.81, p-unif = 0.88). Nonetheless, the distributions of $\langle \Delta\theta/\Delta T \rangle$ for both samples in the jet frame are strongly non-uniform (p-unif < 2 $\times$ 10^{-5}). The power law-like shape of the $\langle \Delta\theta/\Delta T \rangle$ distributions in the jet frame is likely a stochastic outcome of the $T_{\mathrm{rot}}^{\mathrm{jet}}$ and $\Delta\theta_{\mathrm{max}}$ distributions shown in Figs 4 and 5. The following Monte Carlo simulation confirms this assumption: we generated a set of 10^6 rotation amplitudes uniformly distributed between $90°$ and $360°$, and a set of 10^6 rotation durations in the jet frame. The latter set was drawn from the uniform distribution between 19 and 465 d, which corresponds to the parameters found for the full sample in the previous subsection. As will be shown in Section 3.5, the amplitudes and durations of the rotations are not correlated. Therefore, we produced a simulated distribution of $\langle \Delta\theta/\Delta T \rangle_{\mathrm{sim}}$ randomly combining durations and amplitudes from the two generated sets. This distribution cannot be
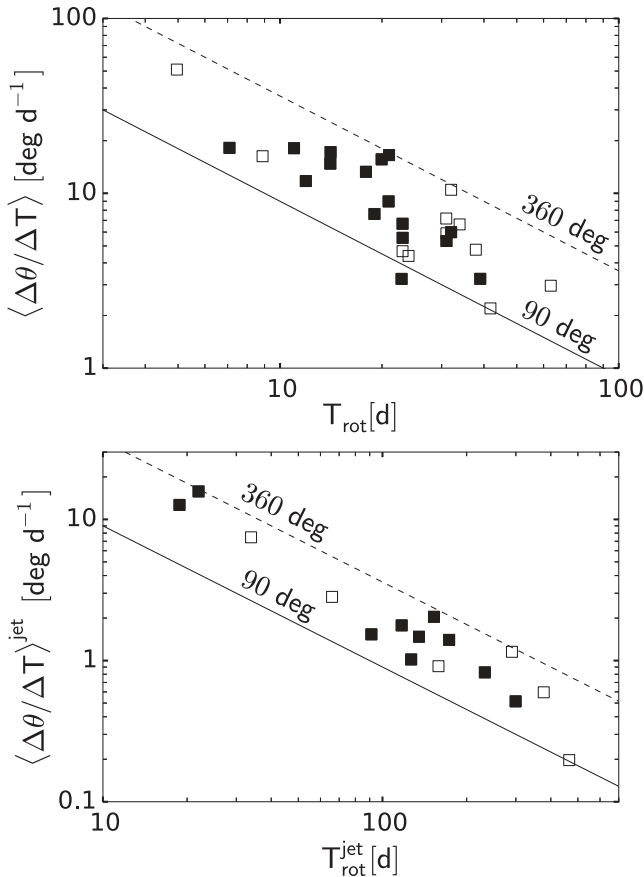
Figure 7. Dependence of rotation rate on T_{rot}: observed values (top) and translated to the comoving frame (bottom). Filled symbols indicate the rotations from the complete sample, which is a subset of the full sample.

distinguished from $\langle \Delta\theta/\Delta T \rangle^{jet}$ for the full sample according to the K–S test (p-value $= 0.57$). Repeating this simulation for the complete sample, we obtained a similar result (p-value $= 0.85$).

3.4 Rate versus duration

Fig. 7 shows a plot of $\langle \Delta\theta/\Delta T \rangle$ versus T_{rot} in the observer frame (top panel) and the jet reference frame (bottom panels), for the full and complete samples (open and filled symbols). The lower left corner in this plot is not populated because of the $90°$ cut in our definition of an EVPA rotation. Any event below the solid line has $\Delta\theta_{max} < 90°$. The single point below this line is the rotation in RBPL J2311+3425 included in the sample despite its $\Delta\theta_{max} = 74°$ (see discussion in Paper I). The dashed line in Fig. 7 corresponds to rotations with $\Delta\theta_{max} = 360°$.

The horizontal cut seen in the observer frame above $\langle \Delta\theta/\Delta T \rangle = 20$ deg d^{-1} appears because faster rotations require higher median cadence of observations in order to be detected, as discussed in the previous subsection. The apparent sparseness in the top left quadrant of the bottom panel of Fig. 7 is partially produced by the same selection effect, while partially it is a consequence of the logarithmic scale representation.

3.5 Amplitude versus duration

Fig. 8 shows the dependences of $\Delta\theta_{max}$ on T_{rot} for the rotations in the observer and jet frames (top and bottom panel) for the full and
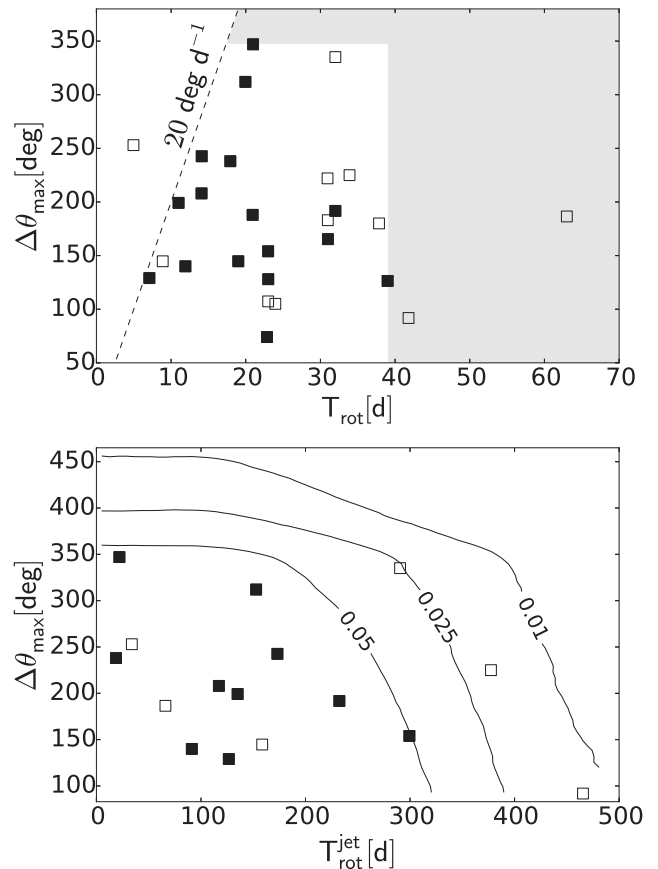

Figure 8. Amplitudes of the rotations versus observed T_{rot} (top) and amplitudes versus T_{rot} in the jet reference frame (bottom). Filled symbols indicate the rotations from the complete sample, which is a subset of the full sample. See the text for details.

complete samples. There is no correlation between the quantities in either of the plots. The corresponding Pearson correlation coefficients for the full sample are $r = -0.04$ in the observer frame and $r = -0.31$ in the jet frame. The absence of correlation holds for the complete sample as well ($r = 0.3$ and 0.42).

The grey area in the top panel of Fig. 8 shows the region limited by $\Delta\theta_{max} > 347°$, $T_{rot} > 39$ d and $\langle \Delta\theta/\Delta T \rangle \leq 20$ deg d^{-1}. We are sensitive to rotations in this region, but none is present in the complete sample.

In order to clarify whether the lack of rotations in this region implies that T_{rot}^{jet} and $\Delta\theta_{max}$ have upper limits, we performed a Monte Carlo simulation. We varied two parameters: the upper limit of amplitudes, $\Delta\Theta$, in the range $(90°, 1000°]$ and the upper limit of durations, $\mathcal{T}$, in the range $(0$ d, 1000 d$]$. For each $(\Delta\Theta, \mathcal{T})$ pair, we generated 10^4 sets consisting of 10 rotations. Parameters of the rotations $\Delta\theta_{max}$ and T_{rot}^{jet} were assumed to be uniformly distributed in the ranges $(0, \Delta\Theta]$ and $(0, \mathcal{T}]$, respectively (see Sections 3.1 and 3.2). The simulated T_{rot}^{jet} measurements were transformed to the observer reference frame values T_{rot} using random $\delta/(1 + z)$ denominators drawn from a uniform distribution in the range $[1, 17.9]$ (see Section 2.3). An additional requirement was added that $\Delta\theta_{max}/T_{rot} \leq 20$ deg d^{-1}. Thereby we simulated the distribution of the $\Delta\theta_{max}$ and T_{rot} in the complete sample for each combination of $(\Delta\Theta, \mathcal{T})$. Then we counted the fraction of the 10^4 sets of simulated rotations for each $(\Delta\Theta, \mathcal{T})$ pair that produced zero rotations in the grey area of the top panel of Fig. 8, i.e. when the simulated sets had

events neither longer in duration nor larger in amplitude than the rotations of the complete sample. The curved lines in the bottom panel of Fig. 8 bound the $(\Delta\Theta, \mathcal{T})$ regions in which more than 5 per cent, 2.5 per cent and 1 per cent of the simulations produced at least one rotation in the grey region of the top panel. In other words, if the EVPA rotations were able to have $T_{\mathrm{rot}}^{\mathrm{jet}} > 500$ d and $\Delta\theta_{\max} > 455°$, then we would expect to have only rotations with $\Delta\theta_{\max} \leq 347°$ and $T_{\mathrm{rot}} \leq 39$ d in the complete sample with probability less than 1 per cent. Thus the values of $\Delta\theta_{\max}$, $T_{\mathrm{rot}}^{\mathrm{jet}}$ and T_{rot} of the rotations in the parent sample are likely to be limited. These limits could be caused by boundaries of the physical parameters in the jet such as size of the emission region, topology of the magnetic field and finite bulk speed of the moving emission features responsible for the EVPA rotations.

4 VARIABILITY OF PARAMETERS DURING EVPA ROTATIONS

4.1 Fractional polarization during EVPA rotations

Here we examine whether the polarization fraction is systematically different during EVPA rotations and in the non-rotating state. We apply a maximum likelihood analysis in order to compute the mean 'intrinsic' polarization fraction p_0, as well as the 'intrinsic' modulation index m_p of the polarization fraction. The method was introduced by Richards et al. (2011) and relies on an assumption about the distribution followed by the desired quantity. In our case, the polarization fraction is assumed to follow a Beta distribution. This distribution is constrained between 0 and 1 and it provides a natural choice for the distribution of polarization fraction. Using the method described in Appendix A, we found the mean 'intrinsic' polarization fraction p_0^{rot} and the modulation index $m_\mathrm{p}^{\mathrm{rot}}$ during the rotations and $p_0^{\mathrm{non\text{-}rot}}$, $m_\mathrm{p}^{\mathrm{non\text{-}rot}}$ for intervals in which no rotations were detected. Then dividing the corresponding values we constructed the distributions shown in Fig. 9.

The distribution of the relative polarization fraction during rotations deviates significantly from a normal distribution (*p*-value $< 10^{-13}$). Out of 27 observed rotations, 18 have $p_0^{\mathrm{rot}}/p_0^{\mathrm{non\text{-}rot}} < 1$, i.e. the mean polarization fraction is lower during the rotations than during the intervals with no rotations. At the same time, the relative modulation index distribution has a mean equal to 0.94 and cannot be distinguished from a normal distribution centred at unity by the K–S test (*p*-value = 0.70). We therefore conclude that most of the rotations are accompanied by a decrease of the fractional polarization, while its variability properties on average remain constant.
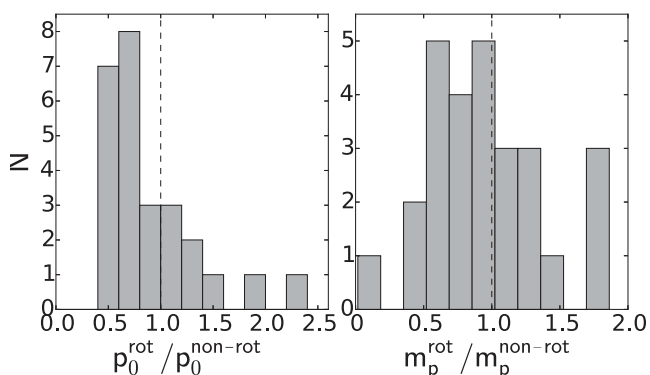

Figure 9. Distributions of the mean relative polarization fraction $p_0^{\mathrm{rot}}/p_0^{\mathrm{non\text{-}rot}}$ and relative modulation index $m_\mathrm{p}^{\mathrm{rot}}/m_\mathrm{p}^{\mathrm{non\text{-}rot}}$.
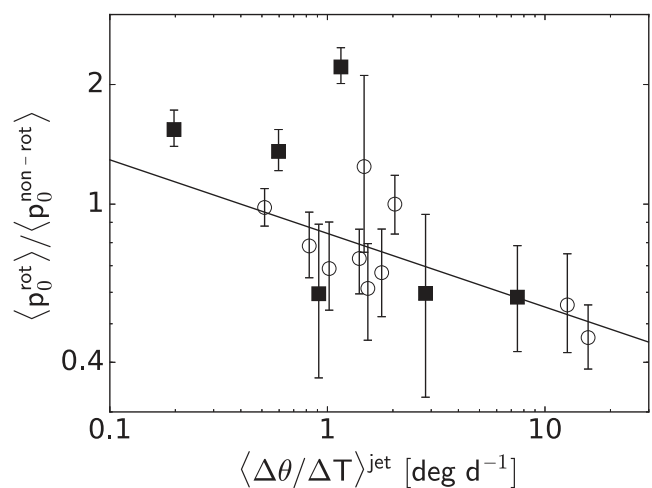

Figure 10. Dependence of $p_0^{\mathrm{rot}}/p_0^{\mathrm{non\text{-}rot}}$ on deboosted and *z*-corrected rotation rate. Rotations of the complete sample are marked by the filled squares. The line shows best linear fit for all the points.

The dependence of $p_0^{\mathrm{rot}}/p_0^{\mathrm{non\text{-}rot}}$ on the rotation rate in the jet reference frame is shown in Fig. 10. The best linear fit to the data, represented by the line, has a slope significantly different from zero, $a = -0.19 \pm 0.07$. The correlation coefficient is $r = -0.66$. In Section 2.3, it was noted that the available Doppler factor estimates used in this paper may be irrelevant to the optical emission region. However, if we randomly shuffle the set of Doppler factors, we can reproduce the 2.7σ significance of the slope in Fig. 10 only in <2 per cent of the trials, implying that the Doppler factors used are physically meaningful.

4.2 Optical total flux density during EVPA rotations

It has been shown that some optical EVPA rotations occur at the same time as flares seen at different frequencies (e.g. Marscher et al. 2008, 2010; Larionov et al. 2013). In Paper I, we showed evidence that for the EVPA rotations and gamma-ray flares, this contemporaneity cannot be accidental in all cases, i.e. at least some of the EVPA rotations are physically related to the closest gamma-ray flares. Here we examine whether the optical flux density is systematically higher during the EVPA rotation events than in the non-rotating state using our large data set. For this purpose, we calculate the average *R*-band flux densities, $\langle F^{\mathrm{rot}}\rangle$ observed during the rotations and $\langle F^{\mathrm{non\text{-}rot}}\rangle$ observed during the rest of each observing season. Then we construct a histogram of $\langle F^{\mathrm{rot}}\rangle/\langle F^{\mathrm{non\text{-}rot}}\rangle$ for all the observed rotations presented in the left-hand panel of Fig. 11. The histogram has a sharp peak at unity, so most of the EVPA rotations do not show any clear increase in the optical flux density. The distribution of $\langle F^{\mathrm{rot}}\rangle/\langle F^{\mathrm{non\text{-}rot}}\rangle$ has mean = 1.12 and $\sigma = 0.45$ and cannot be distinguished from a normal distribution by a K–S test (*p*-value = 0.15).

Nevertheless, there are a number of events where blazars evidently had optical flares during the EVPA rotations. For instance, in two events, RBPL J1048+7143 from the 2013 season (Paper I) and RBPL J1800+7828 (this paper), the average flux density was more than twice as high during the rotations. Another 12 events have $\langle F^{\mathrm{rot}}\rangle/\langle F^{\mathrm{non\text{-}rot}}\rangle > 1$, namely rotations in RBPL J0259+0747, RBPL J1555+1111, RBPL J2202+4216, RBPL J2232+1143 (the first event), RBPL J2243+2021, RBPL J2253+1608 and RBPL J2311+3425 from Paper I, and RBPL J1512−0905 (the second event), RBPL J1748+7005, RBPL J1751+0939,
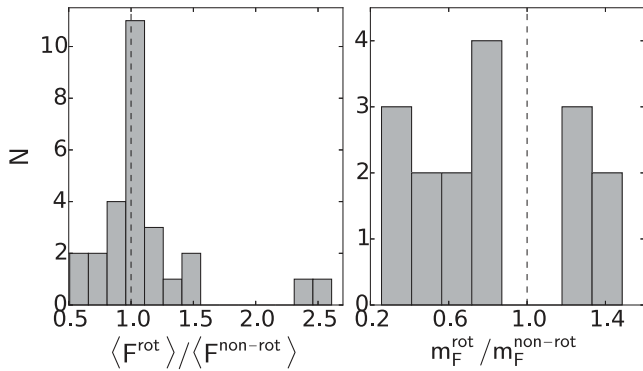
Figure 11. Distribution of $\langle F^{\mathrm{rot}}\rangle/\langle F^{\mathrm{non-rot}}\rangle$ and relative modulation indices $m_F^{\mathrm{rot}}/m_F^{\mathrm{non-rot}}$.

RBPL J1806+6949 and RBPL J2253+1608 from this paper. We notice, however, that some of these events show only a marginal increase of the average flux density during the rotation that cannot be regarded as a clear flare (e.g. RBPL J1512−0905 in Fig. 3).

We have calculated flux density modulation indices m_F^{rot} during and $m_F^{\mathrm{non-rot}}$ outside the EVPA rotation events following Richards et al. (2011). The right-hand panel of Fig. 11 represents the distribution of $m_F^{\mathrm{rot}}/m_F^{\mathrm{non-rot}}$. The EVPA rotations where either m_F^{rot} or $m_F^{\mathrm{non-rot}}$ is undefined or has only an upper limit (due to the lack of measurements or high uncertainties in the flux density) were omitted. This distribution cannot be distinguished from the normal distribution centred at unity by the K–S test (*p*-value = 0.08). Therefore, we conclude that most of the rotations are not accompanied by a simultaneous systematic change of the total flux density in the optical band. The variability properties remain constant on average as well.

4.3 Flux density change versus polarization fraction change during EVPA rotations

The change of the fractional polarization $p_0^{\mathrm{rot}}/p_0^{\mathrm{non-rot}}$ versus the relative flux density $F^{\mathrm{rot}}/F^{\mathrm{non-rot}}$ during the EVPA rotations is presented in Fig. 12. There is no significant correlation between these two parameters ($r = 0.22$, *p*-value = 0.33).
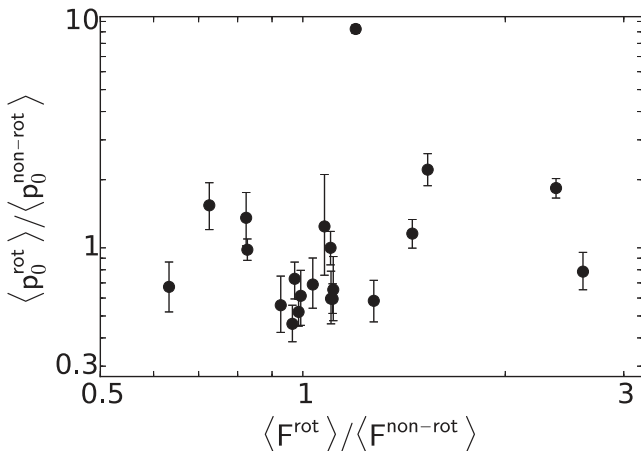

Figure 12. Dependence of the average fractional polarization change on the average flux density change during rotations.

5 DISCUSSION AND CONCLUSIONS

We have analysed the parameters of 27 EVPA rotations detected by RoboPol during two seasons of operation, and we have compared the average flux density and fractional polarization during the rotation events with their values during non-rotating periods, with the following results.

The distribution of $\Delta\theta_{\mathrm{max}}$ cannot be distinguished from a normal or from a uniform distribution. However, there is an apparent peak near the mean (186°) of the distribution. This value is close to $\Delta\theta_{\mathrm{max}} = 180°$, which frequently appears in some simulations (Zhang, Chen & Böttcher 2014; Zhang et al. 2016). It appears because the magnetic field projection is transformed from poloidal to toroidal and back during a passage of a shock through the emission region. Both transitions produce an overall 180° rotation of the EVPA. More than half of the observed rotations (14 out of 27) have $\Delta\theta_{\mathrm{max}} > 180°$. It is difficult to explain these long rotations within a 'bent jet' scenario, since a smooth rotation with the amplitude >180° requires a special configuration of the bend. However, some short rotations can be successfully explained by this model (Abdo et al. 2010; Aleksić et al. 2014).

We found that $\Delta\theta_{\mathrm{max}}$ and T_{rot} do not show any significant correlation either in the full sample or in the complete sample. This lack of correlation is naturally expected if the rotations are produced by a random walk process. It is also expected if the rotations are produced by a moving emission feature, because the corresponding models predict drastic changes of the observed variability of the EVPA, fractional polarization and the total flux density under even small changes of the model parameters (see e.g. Larionov et al. 2013; Zhang et al. 2016). These model parameters, including the Lorentz factor of the moving feature, the viewing angle of the jet, and the pitch angle of the magnetic are different in different blazars, and can change with time even in a single blazar (Raiteri et al. 2010).

The decrease of the polarization during rotations could in principle be explained by the random walk model. The net polarization will be relatively high if the turbulent zone produces only a small fraction of the overall emission in the undisturbed jet, while the part of the jet with ordered magnetic field dominates in the total emission. Then a disturbance passing through the turbulent zone can lead to an enhancement of the emission and thereby decrease the net polarization, while also producing occasional EVPA rotations. However, in this case one would expect to see an increase of the total flux density during rotations, which is observed only in a small fraction of events as we found in Section 4.2, as well as a correlation between the relative average polarization and the relative average flux density during rotations, which is not observed – as discussed in Section 4.3. In the case when the turbulent emission region continuously dominates in the overall emission, the fractional polarization during EVPA rotations is expected to remain unchanged. If the EVPA rotations are produced by an emission feature travelling in the jet with a helical magnetic field, then one would expect to observe an increase of the average polarization fraction during the rotation, because in this case the total emission is dominated by a single component, which occupies a compact region in the jet. A drop in the fractional polarization during EVPA rotations is expected if they are caused by a change of the magnetic field geometry due to a shock passing through the emission region (Zhang et al. 2014, 2016). In this case, a transition from poloidal to toroidal domination takes place in the projected magnetic field leading to depolarization, as shown in simulations by Zhang et al. (2016).

We found that the relative average fractional polarization during the EVPA rotations, $p_0^{\text{rot}}/p_0^{\text{non-rot}}$, is correlated with the rotation rate in the jet reference frame. This dependence is hard to explain within existing models. For the random walk model, we do not expect to see any systematic change of the polarization depending on the rotation rate. For the shock propagating in the jet, a positive correlation is expected, since faster shocks must produce faster rotations, and at the same time must amplify the toroidal component of the magnetic field more efficiently, thereby producing stronger fractional polarization (Zhang et al. 2016). The dependence of $p_0^{\text{rot}}/p_0^{\text{non-rot}}$ on $\langle \Delta\theta/\Delta T \rangle$ can alternatively be produced by two separate populations of the rotations. Signs of these two separate clusters are seen in Fig. 10. One of the populations with $\langle \Delta\theta/\Delta T \rangle > 1$ deg d^{-1} is narrowly distributed around the horizontal line $p_0^{\text{rot}}/p_0^{\text{non-rot}} \approx 0.6$, while the second set of rotations has a wide distribution around $p_0^{\text{rot}}/p_0^{\text{non-rot}} \approx 1$ and has $\langle \Delta\theta/\Delta T \rangle < 2.2$ deg d^{-1}. However, a larger set of EVPA rotations is required to find significant clustering in this plane.

The majority of the rotations do not show any systematic accompanying increase or decrease in the total optical flux density. Moreover, a number of events have been reported in which the EVPA rotation was not accompanied by a flare (e.g. Itoh et al. 2013). This behaviour can be naturally explained if these EVPA rotations are produced by a random walk of the polarization vector caused by the turbulent zone dominating in the overall emission of the jet. On the other hand, events of this kind are also consistent with the passage of shocks through strongly magnetized jets. In this case, mildly relativistic shocks are able to enhance the toroidal component of the magnetic field and thereby produce significant variations of the EVPA and polarization degree, but the flux density does not increase significantly to produce a prominent flare, as shown in simulations by Zhang et al. (2016).

The properties of the complete sample of EVPA rotations with $\langle \Delta\theta/\Delta T \rangle < 20$ deg d^{-1} imply that the parameters $\Delta\theta_{\text{max}}$ and $T_{\text{rot}}^{\text{jet}}$ (and thereby T_{rot}) of the parent distributions are limited in range. The null hypothesis that $\Delta\theta_{\text{max}}$ is able to exceed 360° (460°) is rejected at the significance levels 0.05 (0.01). The null hypothesis that $T_{\text{rot}}^{\text{jet}}$ can be longer than 350 d (500 d) is rejected as well at the corresponding significance levels. These limits are presumably related to a characteristic scale of the zone in the jet responsible for the EVPA rotations, and successful models of the phenomenon will need to take these limits into account.

ACKNOWLEDGEMENTS

REFERENCES

Abdo A. A. et al., 2010, Nature, 463, 919
Aleksić J. et al., 2014, A&A, 567, A41
Angel J. R. P., Stockman H. S., 1980, ARA&A, 18, 321
Blinov D. et al., 2015, MNRAS, 453, 1669 (Paper I)
Clarke D., 2009, Stellar Polarimetry. Wiley-VCH, Weinheim
Gabuzda D. C., Rastorgueva E. A., Smith P. S., O'Sullivan S. P., 2006, MNRAS, 369, 1596
Ghisellini G., Tavecchio F., Foschini L., Ghirlanda G., 2011, MNRAS, 414, 2674
Gómez J. L. et al., 2016, ApJ, 817, 96
Hovatta T., Valtaoja E., Tornikoski M., Lähteenmäki A., 2009, A&A, 494, 527
Itoh R. et al., 2013, ApJ, 768, L24
Kiehlmann S. et al., 2013, EPJ Web Conf., 61, 6003
King O. G. et al., 2014, MNRAS, 442, 1706
Lähteenmäki A., Valtaoja E., 1999, ApJ, 521, 493
Larionov V. M. et al., 2013, ApJ, 768, 40
Marscher A. P. et al., 2008, Nature, 452, 966
Marscher A. P. et al., 2010, ApJ, 710, L126
Monet D. G. et al., 2003, AJ, 125, 984
Moore R. L. et al., 1982, ApJ, 260, 415
Ofek E. O. et al., 2012, PASP, 124, 854
Pavlidou V. et al., 2014, MNRAS, 442, 1693
Raiteri C. M. et al., 2010, A&A, 524, A43
Readhead A. C. S., 1994, ApJ, 426, 51
Richards J. L. et al., 2011, ApJS, 194, 29
Richards J. L., Hovatta T., Max-Moerbeck W., Pavlidou V., Pearson T. J., Readhead A. C. S., 2014, MNRAS, 438, 3058
Sasada M. et al., 2011, PASJ, 63, 489
Schlafly E. F., Finkbeiner D. P., 2011, ApJ, 737, 103
Serkowski K., Mathewson D. S., Ford V. L., 1975, ApJ, 196, 261
Shaw M. S. et al., 2013, ApJ, 764, 135
Uemura M. et al., 2010, PASJ, 62, 69
Zhang H., Chen X., Böttcher M., 2014, ApJ, 789, 66
Zhang H., Deng W., Li H., Böttcher M., 2016, ApJ, 817, 63

APPENDIX A: INTRINSIC AVERAGE POLARIZATION FRACTION AND VARIABILITY AMPLITUDE

We use a likelihood approach to compute the mean intrinsic polarization fraction p_0 and the intrinsic variability amplitude (modulation index m_p), as well as their uncertainties, for a source with intrinsic variable polarization fraction p_i (note that the subscript 'i' is used to denote 'intrinsic').

We assume that the measurements of p_i – if one could observe the source with infinite accuracy, uniformly and over infinite time – would follow a Beta distribution. In that case, the probability density function, is given by

$$\text{pdf}(p_i; \alpha, \beta) = \frac{p_i^{\alpha-1}(1 - p_i)^{\beta-1}}{B(\alpha, \beta)}, \quad (A1)$$

where p_i is confined to $0 \leq p_i \leq 1$ as it should be. There is a peak in the Beta distribution, if the shape parameters α and β are restricted to $\alpha, \beta > 0$. The mean and the variance are given by

$$\mu = \frac{\alpha}{\alpha + \beta} \quad (A2)$$

and

$$\text{Var} = \frac{\alpha\beta}{(\alpha + \beta)^2(\alpha + \beta + 1)}, \qquad (A3)$$

respectively. Thus the mean intrinsic polarization fraction p_0 and the modulation index m_p will be

$$p_0 = \frac{\alpha}{\alpha + \beta} \qquad (A4)$$

and

$$m_p = \frac{\sqrt{\text{Var}}}{\mu} = \frac{\sqrt{\frac{\alpha\beta}{(\alpha+\beta)^2(\alpha+\beta+1)}}}{\frac{\alpha}{\alpha+\beta}}. \qquad (A5)$$

The shape parameters α and β in equation (A1) can be expressed in terms of p_0 and m_p by inverting equations (A4) and (A5), giving

$$\alpha(p_0, m_p) = \left(\frac{1 - p_0}{p_0 m_p^2} - 1\right) p_0 \qquad (A6)$$

and

$$\beta(p_0, m_p) = \left(\frac{1 - p_0}{p_0 m_p^2} - 1\right)(1 - p_0). \qquad (A7)$$

Given p_0 and m_p, the probability density for measuring p_i as a result of intrinsic variability is thus given by

$$\text{pdf}(p_i; p_0, m_p) = \frac{p_i^{\alpha(p_0, m_p)-1}(1 - p_i)^{\beta(p_0, m_p)-1}}{B[\alpha(p_0, m_p), \beta(p_0, m_p)]}. \qquad (A8)$$

Equation (A8) gives the probability density for the polarization fraction of a source to have the value p_i at some instant in time if its average polarization fraction is p_0 and it varies with a modulation index m_p.

Next, we examine the effect of measurement uncertainty. If we assume that the source intrinsic polarization fraction at some instant in time is indeed p_i, then the probability of the experimentally observed polarization degree p_{exp} is given by the Rice distribution (Clarke 2009)

$$P(p_{exp}, p_i, \sigma) = \frac{p_{exp}}{\sigma^2} \exp\left[-\frac{p_{exp}^2 + p_i^2}{2\sigma^2}\right] I_0\left(\frac{p_{exp}p_i}{\sigma^2}\right), \qquad (A9)$$

where σ is the uncertainty of observations[3] and I_0 is the zeroth-order modified Bessel function of the first kind. Equation (A9) is then remedying the effect of the measurement uncertainty.

We can now convolve the two effects. We assume a source with intrinsic mean polarization p_0 and intrinsic polarization modulation index m_p, and we wish to compute the probability to measure p_{exp} if the measurement uncertainty is σ and provided that the true polarization fraction of the source at the time of interest is p_i. This probability is equal to the product of the probabilities given by equations (A8) and (A9),

$$P(p_{exp}, p_0, m_p, p_i, \sigma) = \frac{p_i^{\alpha(p_0, m_p)-1}(1 - p_i)^{\beta(p_0, m_p)-1}}{B(\alpha(p_0, m_p), \beta(p_0, m_p))} \frac{p_{exp}}{\sigma^2}$$
$$\times \exp\left[-\frac{p_{exp}^2 + p_i^2}{2\sigma^2}\right] I_0\left(\frac{p_{exp}p_i}{\sigma^2}\right). \quad (A10)$$

The probability then to observe p_{exp} from a source with p_0 and m_p, though any p_i that the source may be emitting, is

$$P(p_{exp}, p_0, m_p, \sigma) = \int \left\{ \frac{p_i^{\alpha(p_0, m_p)-1}(1 - p_i)^{\beta(p_0, m_p)-1}}{B(\alpha(p_0, m_p), \beta(p_0, m_p))} \frac{p_{exp}}{\sigma^2} \right.$$
$$\left. \times \exp\left[-\frac{p_{exp}^2 + p_i^2}{2\sigma^2}\right] I_0\left(\frac{p_{exp}p_i}{\sigma^2}\right) \right\} dp_i. \quad (A11)$$

Consequently, the likelihood l_j to observe $p_{exp,j}, \sigma$ from a measurement j will be

$$l_j(p_{exp,j}, p_0, m_p, \sigma_j) = P(p_{exp,j}, p_0, m_p, \sigma_j). \qquad (A12)$$

For n independent measurements of our source, the likelihood is

$$\mathcal{L}(p_0, m_p) = \prod_{j=1}^{n} l_j(p_{exp,j}, p_0, m_p, \sigma_j). \qquad (A13)$$

Taking the logarithm of equation (A13) we obtain

$$\log\left[\mathcal{L}(p_0, m_p)\right] = \sum_{j=1}^{n} \log\left[l_j(p_{exp,j}, p_0, m_p, \sigma_j)\right]. \qquad (A14)$$

One can then insert the observed $p_{exp,j}$ and σ_j in equation (A14) or equation (A13), maximize the likelihood and obtain the maximum-likelihood values for p_0 and m_p.

The last necessary step is the estimation of the confidence intervals for p_0 and m_p. This has to be done separately for the two parameters. First, we compute the marginalized likelihood of m_p by integrating over p_0,

$$\mathcal{L}(m_p) = \int \mathcal{L}(p_0, m_p) dp_0. \qquad (A15)$$

Then we compute the integral over all values of m_p to get the normalization of the likelihood for m_p,

$$A = \int_0^\infty \mathcal{L}(m_p) dm_p. \qquad (A16)$$

Starting from a pair of values $m_{p,min}$ and $m_{p,max}$ that equidistantly bracket the maximum likelihood for m_p, we gradually stretch the interval $[m_{p,min}, m_{p,max}]$ until the condition

$$\int_{m_{p,min}}^{m_{p,max}} \mathcal{L}(m_p) dm_p = 0.683A \qquad (A17)$$

is satisfied. The intrinsic modulation index m_p will be given as

$$m_p \pm \frac{m_{p,max} - m_{p,min}}{2}. \qquad (A18)$$

An identical procedure using the marginalized likelihood $\mathcal{L}(p_0) = \int \mathcal{L}(p_0, m_p) dm_p$ is used to calculate uncertainties for p_0. Although we do not compute upper limits for m_p and p_0 in this work, such limits can also be calculated using the marginalized likelihoods above. For example, a 2σ upper limit for m_p could be the value $m_{p,up}$ for which

$$\int_0^{m_{p,up}} \mathcal{L}(m_p) dm_p = 0.955A. \qquad (A19)$$

---

[3] σ is equal to the uncertainty in measuring the Stokes parameters Q and U, assuming the two uncertainties are equal, which is a good approximation if the degree of polarization is low.

This paper has been typeset from a TeX/LaTeX file prepared by the author.